Tellus
SERIES A
DYNAMIC
METEOROLOGY
AND OCEANOGRAPHY
PUBLISHED BY THE INTERNATIONAL METEOROLOGICAL INSTITUTE IN STOCKHOLM

Tellus (2011), 63A, 828–840

TELLUS

Large-scale processes governing the seasonal variability of the Antarctic sea ice

By NORIAKI KIMURA[1]* and MASAAKI WAKATSUCHI[2], [1]*Graduate School of Frontier Sciences, The University of Tokyo, Kashiwa, Japan*; [2]*Institute of Low Temperature Science, Hokkaido University, Sapporo, Japan*

(Manuscript received 12 June 2009; in final form 13 April 2011)

ABSTRACT

The seasonal variability of sea-ice cover in the Southern Ocean is examined using daily sea-ice concentration and ice velocity products for 2003–2009, derived from Advanced Microwave Scanning Radiometer for EOS (AMSR-E) data. This study quantitatively shows the contribution of (1) ice production/reduction within the sea ice, (2) ice production/reduction at the sea-ice edge and (3) zonal ice transport to the seasonal change of sea-ice area. Area of greatest ice production occurs along the coast of Ross Sea and East Antarctica from March to September. The contribution of zonal transport to the seasonal change of ice area is one order magnitude smaller than local ice production/reduction. Clear regional and seasonal differences are found in the large-scale processes named above. Generally, ice area increases due to ice production, both at the ice edge and within the pack in the autumn and winter. The most significant ice production at the ice edge occurred in the Weddell Sea; the ice production provides 56% of total increase of ice cover in this area. In contrast, moderate ice melting occurs at the ice edge through almost all months in the Indian Ocean sector.

1. Introduction

Sea ice is a vital component of the global climate system. When sea ice forms, latent heat is released to the atmosphere and ocean, and brine-rejection increases the salinity of the underlying ocean. When sea ice melts it absorbs latent heat from the nearby air and water, and supplies fresh water to the ocean surface. Importantly, the salt rejection caused by the active sea ice formation over the coastal shelf produces Dense Shelf Water (e.g. Gill, 1973), which is responsible for the formation of Antarctic Bottom Water (AABW).

Around Antarctica, the majority of sea ice is seasonal, forming from early autumn through early spring, and then melting from late spring through summer. This leads to the dramatic seasonal changes, as the total sea-ice extent grows from a minimum of nearly 3.0×10^6 km^2 in late summer to a maximum of nearly 20.0×10^6 km^2 (Gloersen et al., 1992). With recent attention to changes in sea ice cover in the context of climate change (e.g. Vinnikov et al., 2006) a greater understanding of the processes controlling sea-ice extent is required.

Since 1972, observations using satellite microwave sensors have provided continuous images of sea ice over the Northern and Southern Hemisphere, greatly improving our knowledge of sea-ice cover and its temporal and spatial variability (e.g. Parkinson, 1992; 1994). Previous studies have focused on a variety of timescales, namely: daily (e.g. Kimura, 2007), intraseasonal (e.g. Baba et al., 2006), annual (e.g. Enomoto and Ohmura, 1990), interannual (e.g. Zwally et al., 2002) and secular (e.g. Cavalieri et al., 2003). The Japanese AMSR-E sensor on NASA's Aqua satellite launched in May 2002 provides finer spatial resolution than earlier passive microwave sensors and enables high-resolution analyses of sea ice change (e.g. Massom et al., 2008).

Sea ice area changes through both thermodynamic and dynamic processes. Thermodynamic processes contain the production and melting of sea ice, whereas dynamic processes involve the transport and deformation (rafting and ridging) of sea ice. The spatial and temporal difference in the contribution of both the dynamic and thermodynamic processes around Antarctica, and the underlying mechanisms responsible for these patterns have been examined by some numerical model studies (e.g. Fichefet and Maqueda, 1997). However study of large-scale processes through data analysis is very sparse.

This study divides the cause of change in ice area into three processes: (1) ice production and reduction within the sea ice, (2) ice production and reduction at the ice edge and (3) sea-ice transport, and aims to quantify the contribution of these processes to the seasonal change of regional sea-ice area. The distinction between 1 and 2 helps us to define regional differences in the mechanisms governing the seasonal change. For example, ice

*Corresponding author.
e-mail: kimura@1.k.u-tokyo.ac.jp
DOI: 10.1111/j.1600-0870.2011.00526.x

reduction at the ice edge in the advance season implies that thermodynamic conditions are unfavourable and dynamic offshore ice drift is required to expand the ice area. An important point is the term 'reduction' in this study shows apparent decrease of ice area; it includes the redistribution through dynamic deformation of ice floes, which does not always relate to ice melting.

This study focuses only on two-dimensional ice area and not the three-dimensional volume of sea ice, because to-date satellite observations cannot measure the thickness of sea ice in sufficient accuracy and there is insufficient in situ observations. Despite this restriction, we believe that this study is valuable, because the impact of sea ice on climate depends strongly on whether sea ice exists or not, and achievements of this study would be valuable to understand mechanism controlling the seasonal variation of ice area and to validate and improve the large-scale numerical model.

In this paper, Section 2 explains the data and methods used. Section 3 describes the seasonal and regional distribution of specific ice processes. Section 4 details the contribution of the ice processes responsible for the seasonal variability of ice area. Finally, the summary and discussion are given in Section 5.

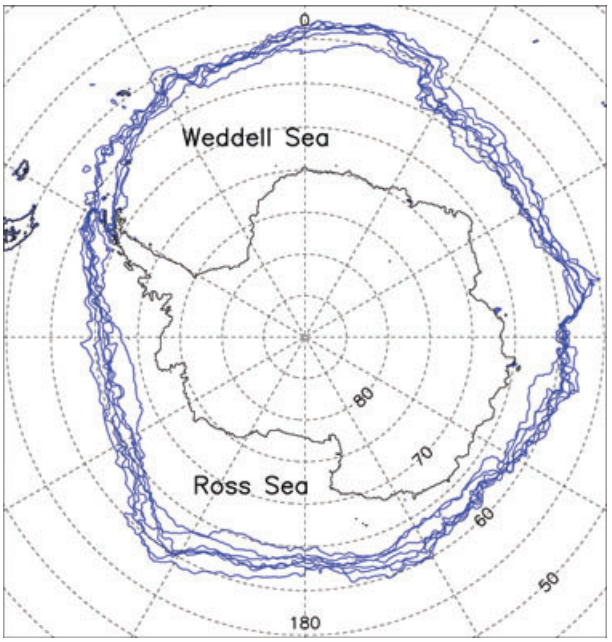

Fig. 1. Maximum ice-edge locations for 2003–2009.

2. Data

In this study, we use passive microwave signatures from images gathered by the AMSR-E onboard the Aqua satellite. The AMSR-E measures at six frequencies from 6.9 to 89 GHz at both horizontal and vertical polarization. The gridded daily brightness temperature is binned to square pixels of 6.25 × 6.25 km (89 GHz channel) or 12.5 × 12.5 km (lower frequency observations) distributed by the National Snow and Ice Data Center (NSIDC). Two types of sea-ice products are prepared for this study: sea-ice concentration and sea-ice velocity.

Ice concentration used in this study is the product derived and distributed by NSIDC, calculated using the Enhanced NASA Team (NT2) algorithm (Markus and Cavalieri, 2000). Figure 1 shows the maximum Antarctic sea-ice extent, defined as 15% of ice concentration, for 2003–2009. Interannual variability of ice extent is relatively small; difference in the meridional ice edge location is within a range of 5°. Overall the pattern of Antarctic sea-ice extent is maintained across all years. In general, the sea-ice area expands northward in the region 30°W–30°E and around 150°W, while between 90°E–150°E and 60°W–120°W, the sea-ice area is limited to a narrower band. In this study, we will mainly focus on the regional and seasonal change in ice area.

Ice velocity is computed from the horizontal and vertical polarization channel of 89 GHz on AMSR-E. Twice-daily (ascending and descending) data is available by NSIDC. This channel is affected by some weather conditions such as thick cloud cover. Then the calculated ice velocity seems to be slightly biased toward ice condition under the clear sky environment. The reason for the use of 89 GHz channel is that it provides the highest spatial resolution and thus is most effective for mapping ice motion. The procedure for detecting ice motion is based on the maximum cross-correlation method described in Ninnis et al. (1986) and Emery et al. (1991). This method determines the spatial offset that maximizes the cross-correlation coefficient between two brightness temperature arrays in consecutive images separated by 24 h. Calculations are carried out from ascending to ascending and from descending to descending images. For this procedure, 6 × 6 (37.5 × 37.5 km) pixel arrays are utilized. Regions including land or open ocean pixels are masked out based on the ice concentration data. Detections of a false match are automatically filtered out using the maximum cross-correlation coefficient, sharpness of the correlation peak, and the consistency with displacement vectors in the neighbourhood. After filtering, we constructed a daily-averaged ice-velocity data set on a 37.5 × 37.5 km grid for 2003–2009. The daily data for any given grid point is calculated as a mean value of four data derived from the horizontal polarization channel image of ascending and descending data, and the vertical polarization channel image of ascending and descending data. By comparison between the ice tracks calculated from this data set and tracks of ice floes detected on National Oceanic and Atmospheric Administration (NOAA) Advanced Very High Resolution Radiometer (AVHRR) image, we found that the floe speed is 40% faster than the AMSR-E derived ice speed. This underestimation agrees well with a difference between ice motions derived from Special Sensor Microwave Imager (SSM/I) data and drifting buoys shown by Heil et al. (2001). Based on these results, ice velocity products used in this study are simply multiplied by a factor 1.4 throughout all period. Concerning the angle of the velocity, there is no

significant via in the AMSR-E derived ice motion. The following analyses are carried out using this product for 7 yr of AMSR-E observation between 2003 and 2009.

3. Processes influencing sea ice area

3.1. Seasonal variability

Figure 2 shows the monthly change in sea-ice concentration around Antarctica: for example, the value for January indicates that sea-ice area decreased during the month, defined by the difference in ice concentration between February 1 and January 1. This calculation is carried out for each month over the 7 yr of 2003–2009 and then averaged. In general ice area increases from March to September and reaches a maximum in most regions in September. Ice area decreases from October to February. Decrease rate is largest in December, especially in the Weddell Sea with an ice reduction of over 50% of ice concentration during that month.

Error in the derived value depends on the error in ice concentration. Cavalieri et al. (2006) reported that bias of it ranged from 0 to 3% and a root mean square error ranges from 1 to 7%. Since typical value of the monthly change of ice area (*CA*) is based on tens of percentage point, the value representing *CA* error is within the range of a single digit percentage numbers.

Monthly change of ice area (*CA*) in any given region occurs through the ice production within the sea-ice (*PI*), ice reduction within the sea ice (*RI*), ice production at the ice edge (*PE*), ice reduction at the ice edge (*RE*), inflow from the adjoining region (*IF*) and outflow to the adjoining region (*OF*). These abbreviations are summarized in Table 1. As stated in the previous section, *RI* contains not only thermodynamic ice melting

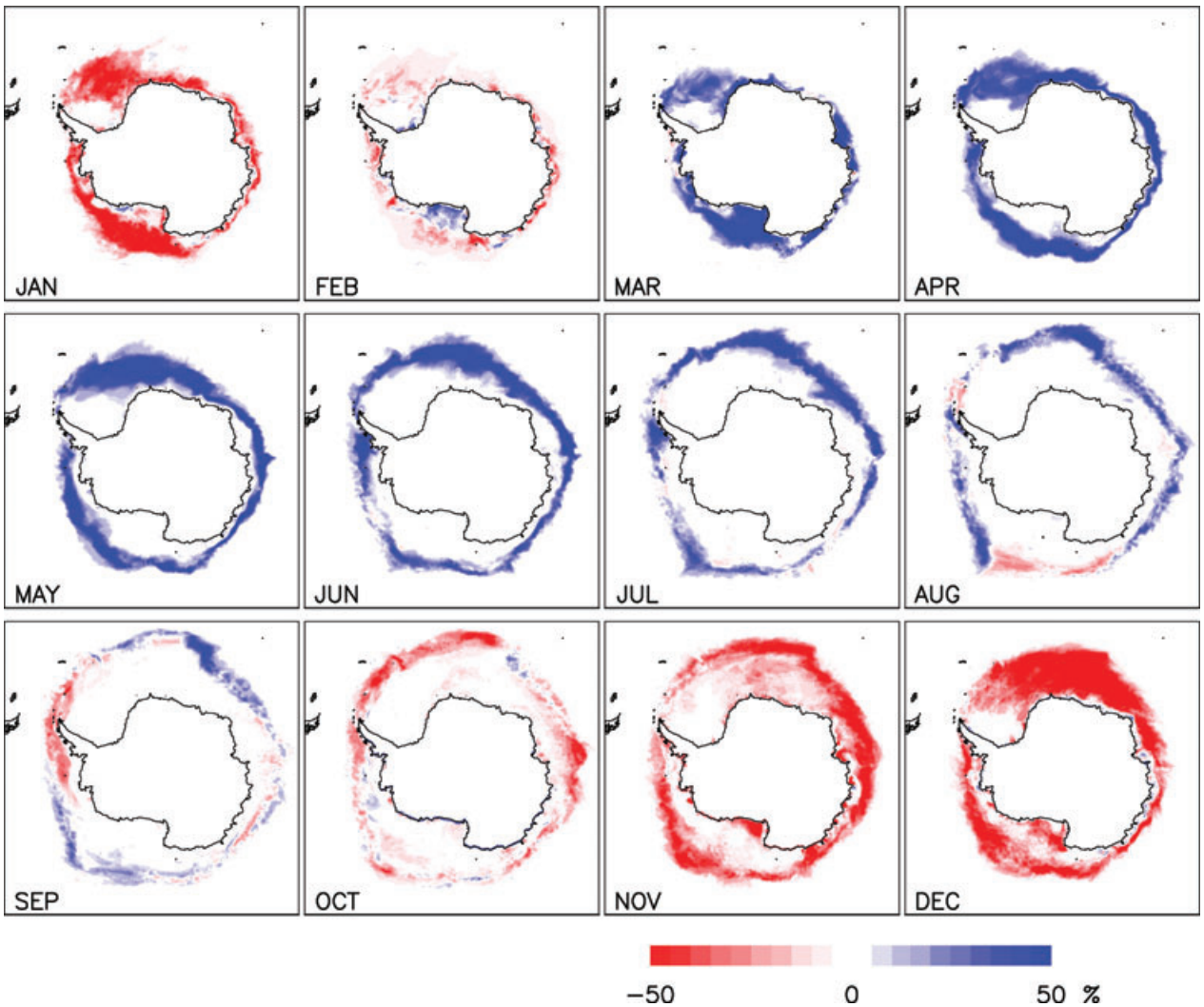

Fig. 2. Change in sea ice concentration during each month calculated by subtracting the ice concentration at the first day of next month from the first day of each month.

Table 1. Abbreviation for specific ice processes

CA	Change in ice area
PI	Ice production within the sea ice
RI	Ice reduction within the sea ice
IF	Inflow from adjoining areas
OF	Outflow to adjoining areas
PE	Ice production at the ice edge
RE	Ice reduction at the ice edge

but also decrease of ice area due to redistribution by dynamic deformation, which is not always accompanied by decrease of ice volume. These factors should be balanced in any region as follows:

$$CA = (PI - RI) + (PE - RE) + (IF - OF). \quad (1)$$

This study aims to reveal the contribution of terms in (1) in each month. Since CA, PI, RI, IF and OF can be derived from the ice concentration and ice velocity products, net ice production at the ice edge ($PE - RE$) can be derived by the balance of these terms.

3.2. Ice production/reduction within the sea ice

A key of this study is estimation of ice production and reduction within the sea ice from the daily ice concentration and ice velocity. For the estimation we focus on any given unit pixel (37.5 × 37.5 km size) enclosed by adjacent grids. This study adopts a calculation method used in Kimura and Wakatsuchi (2004) that assumes that the sea-ice area changes in response to local ice production/reduction and ice convergence/divergence. We can relate the observed increase of sea-ice area in a given pixel to the sum of ice production in that pixel and the advection of sea ice from the surrounding pixels due to ice convergence. The increased area due to ice production [$P(t)$] in a pixel is calculated by

$$P(t) = [A(t+1) - A(t)] - Fin(t), \quad (2)$$

where $A(t)$ is the daily ice-covered area calculated as the ice concentration multiplied by the area of the pixel (37.5 × 37.5 km^2), $A(t+1)$ is the same ice area for the next day, $Fin(t)$, which is also calculated using the daily ice concentration and velocity, is the area of ice advected in from the adjoining pixels. Positive and negative $Fin(t)$ correspond to convergence and divergence of the ice field, respectively. Taking, for example, typical situation of the ice production in a coastal polynya or lead accompanied by ice divergence, if the ice concentration at a given pixel does not change (i.e. when $A(t+1) - A(t) = 0$), the produced ice area $P(t)$ takes a positive value in the case of ice divergence [$Fin(t) < 0$]. Positive $P(t)$ indicates thermodynamic ice production within the polynya or lead within the sea ice.

This way of estimation can detect the ice production occurring in smaller or narrower area than the data resolution (37.5 km): coastal polynya, lead, and other small opening accompanied by large-scale ice divergence. However, we cannot detect ice production and reduction due to smaller-scale or shorter time-scale ice divergence/convergence. If ice production and reduction occur concurrently, the absolute value of $P(t)$ becomes underestimated. This problem becomes critical in areas that small-scale complex ice process is prevailing, such as undulating pancake ice field where small-scale divergence and convergence field are formed adjacently or areas where tidal and internal oscillations make up a significant portion of ice motion and deformation.

Net ice production within the sea ice ($PI - RI$) is calculated as spatial or temporal sum of $P(t)$. $P(t)$ also contain error due to errors in ice velocity and ice concentration. Especially, error in ice velocity results in the large error of $P(t)$, because $P(t)$, which largely depends on ice divergence, is sensitive to small error in the velocity. The error is accumulated into both PI and RI as a large overestimate. However in the net ice production of $PI - RI$, most of the overestimate in the products is cancelled out between PI and RI. As a result, error in monthly $PI - RI$ is evaluated as 20.7% in the end of Section 4.

Another important point is that the method to calculate $P(t)$ is limited to the interior of the sea ice and is not applied at the sea-ice edge. This study defines the area within the sea ice as interior of pack excluding the part within 37.5 km from ice edge. In the calculation process of $P(t)$, we do not take a pixels within one grid-size (37.5 km) from the ice edge into consideration. This treatment enables us to distinguish the $PE - RE$ from PI and RI. Though $PE - RE$ is not calculated directly; it is calculated by the balance of (1) as $CA - (PI - RI) - (IF - OF)$. The derived $PE - RE$ includes net ice production at the sea-ice edge involving sea ice interior within one pixel (37.5 km) from the ice edge.

Figure 3 displays the annual map of net ice production within the sea ice (PI–RI) per unit area averaged over 2003–2009. It was calculated for each pixel in the following way. First, daily $P(t)$ was calculated from ice concentration and velocity data. Next, $P(t)$ was summed over the 7 yr, and then divided by the number of days excluding those associated with missing data. Finally, the mean of $P(t)$ was multiplied by the total number of days of ice existence. The resulting $PI - RI$ reflects both the ice productivity and the duration of ice cover. Based on Fig. 3, 8.3×10^7 km^2 of ice area is produced within the sea ice during 1 yr. The positive value of the total $PI - RI$ implies that ice melting at the ice edge (RE) is larger than ice production at the ice edge (PE) because the annual total ice production ($PI + PE$) should be equal to total ice reduction ($RI + RE$).

The highest ice production occurs in the coastal regions, and in particular those of the Ross Sea, where 12.5×10^5 km^2 of ice area is produced during 1 yr within the blue rectangle labelled 'R' in Fig. 3. High productivity is also detected around the Eastern Hemisphere, especially in known active ice production regions

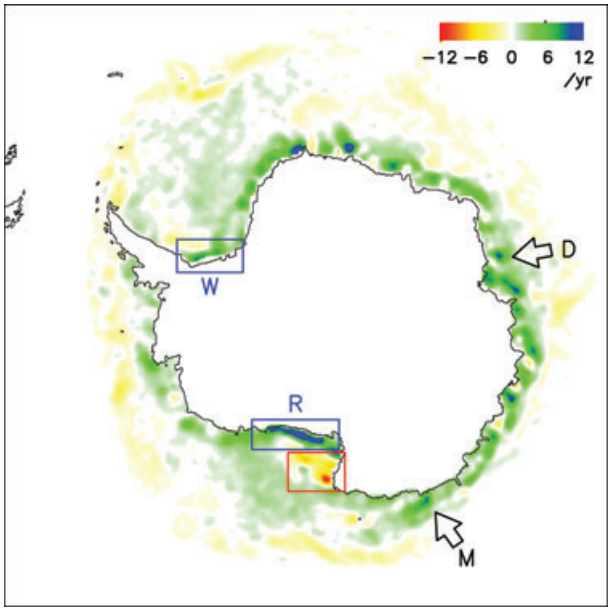

Fig. 3. Spatial distribution of net ice production per unit area during one year averaged over 2003–2009. For example, value of 8.0 represents that 8.0 km^2 of ice area is produced in a 1.0 km^2 of area during 1 yr. Blue rectangles labeled 'R' and 'W' define the Ross Sea and Weddell Sea polynya area, respectively. Red rectangle defines a convergence area. Arrows labeled 'M' and 'D' indicate the location of Mertz Glacier polynya and Cape Darnley polynya, respectively.

such as the Mertz Glacier polynya (Rintoul, 1998; Marsland et al., 2004) shown by an arrow labelled 'M', and Cape Darnley polynya (Tamura et al., 2008) shown by an arrow labelled 'D'. These ice production occurs in downstream area of projections of coastline such as capes. This characteristics also is seen in the model result by Kusahara et al. (2010). In addition, we can find ice reduction due to ice convergence in upstream area of them. The high productivity areas are also found around the coast of the eastern Weddell Sea (near 0° meridian) especially in the east side of capes. Overall distribution of high production areas is similar to the map of annual ice production in coastal polynyas shown in Tamura et al. (2008), estimated by a thermodynamic calculation. Ice production in the coastal polynya of the Weddell and Amundsen-Bellingshausen Seas is not large. In the blue rectangle labelled 'W' in the Weddell Sea, a smaller 3.5 × 10^5 km^2 of ice area is produced during 1 yr. On the other hand, high ice reduction area is notable in the Ross Sea as shown by the red rectangular; this is likely to be due to dynamic deformation of sea ice because this area is a convergence area of sea ice. In the rectangle, 6.6 × 10^5 km^2 of ice area is decreased during 1 yr.

Figure 4 shows the interannual change of net ice production in the Ross and Weddell coastal areas (blue rectangles 'R' and 'W' in Fig. 3). Though there is no distinct interannual change in the ice production in the Weddell coastal area, ice production in the Ross coastal area shown by a red line becomes small with

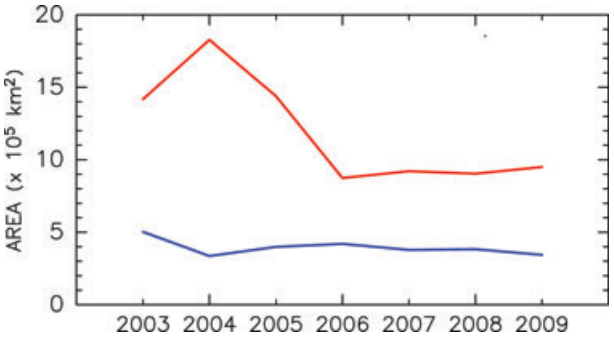

Fig. 4. Interannual change of net ice production in the Ross (red line) and Weddell (blue line) coastal areas defined by blue rectangles in Fig. 3.

year; area of ice production after 2006 are nearly half of it before 2005. This reduction should have an impact on the formation of saline water and possibly relates to a salinization of the shelf water in the Ross Sea (Jacobs and Giulivi, 2010).

Figure 5 shows the monthly breakdown of the results in Fig. 3 and confirms that ice production is active in the growth season of April–September, in both the coastal and offshore regions. The Ross Sea polynya has the longest duration of active sea-ice production from March to October. Ice production in off-shore areas is evident in March to September, and changes to ice reduction from October to December. Though the offshore area is characterized by lower ice productivity compared with the coastal area, it still plays an important role in the increase of ice area because the offshore ice area has a larger coverage. For example, a large amount of sea ice is produced in the offshore ice area of the Weddell Sea (shown in Section 4) where is characterized by low ice productivity in the coastal area. This result represents the importance of the ice production in lead or other small opening in the interior pack (e.g. Eisen and Kottmeier, 2000), which is not resolved explicitly by AMSR-E resolution. Ice reduction is dominant during the melt season of November–January. Large melting in this season is consistent with Nihashi et al. (2005), which shows that ice melting within the sea ice is an important process in the seasonal decay of ice extent. It should be noted that sea ice deformation is an important process in the Antarctic (e.g. Worby et al., 1996), and the seasonal decay occurs not only by a gentle ice melting but also by a strong contribution of small-scale dynamical processes (Geiger and Perovich, 2008). Ice reduction shown in this study involves both contributions.

3.3. Zonal Sea Ice Transport

Changes in regional ice area is a function of not only the *in situ* thermodynamics and dynamic deformation, but also the transport of sea ice (*IF* and *OF*) from adjoining areas. The zonal transport of sea ice around Antarctica is calculated using the daily sea ice concentration and zonal ice-drift speed. Figure 6 shows the annual values of zonal transport in 30° intervals of longitude around Antarctica. The mean sea ice transport is

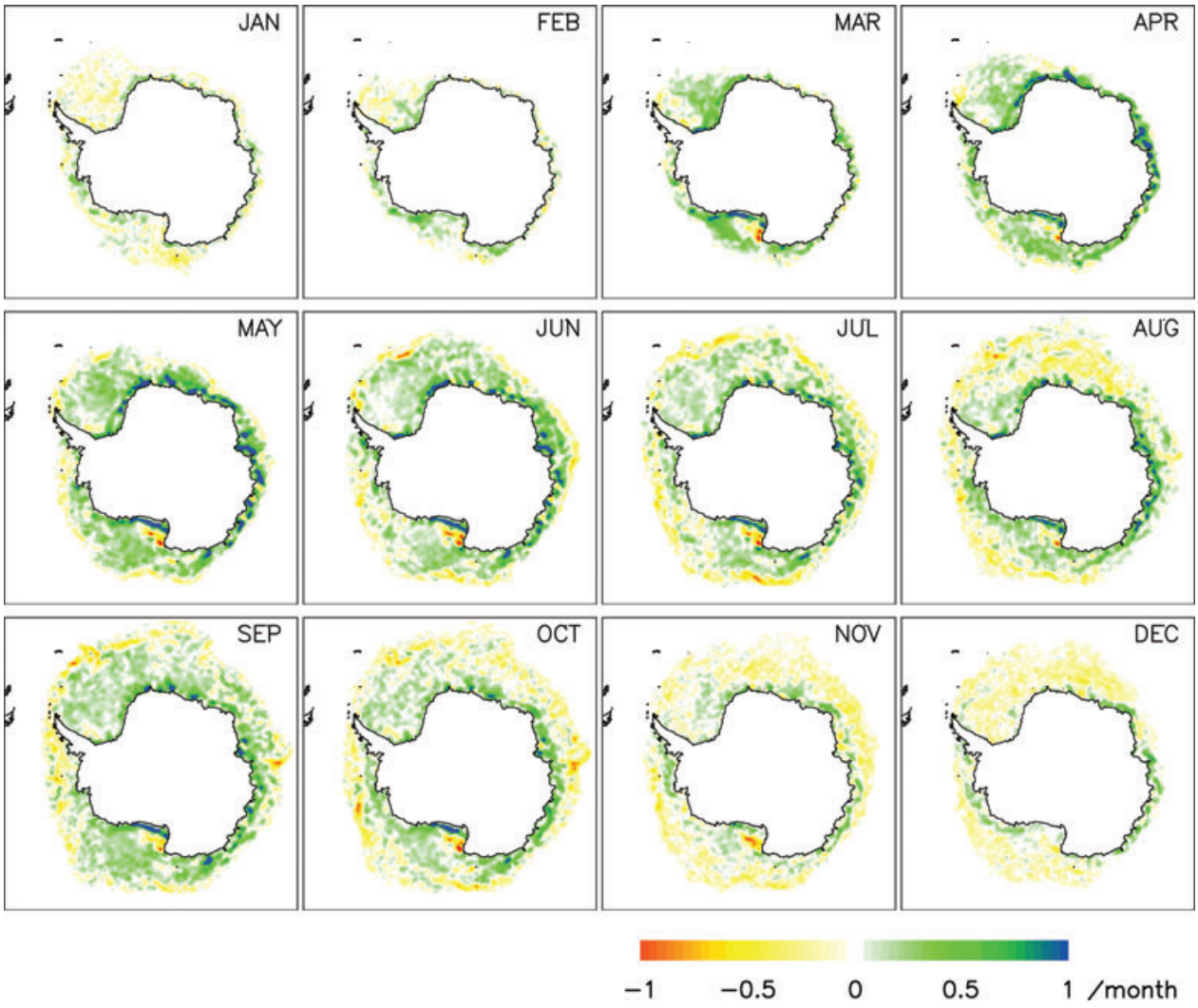

Fig. 5. Same as Fig. 3, but for each month.

eastward and westward in the western (0°–90°W–180°) and eastern (0°–90°E–180°) hemispheres, respectively. This direction is produced by the mean ice motion field, which is characterized by eastward circumpolar drift, northward drifts in the Weddell Sea and Ross Sea, and narrow westward coastal currents (Emery et al., 1997; Kimura, 2004); the predominant westward coastal current rather than the eastward circumpolar drift results in the net ice transport being westward in the eastern hemisphere. The largest transports are located in the eastern Weddell (beyond 0° meridian) and eastern Ross Seas (beyond 150°W meridian) reflecting the strong Weddell Gyre (Gordon et al., 1981) and Ross Sea Gyre. The eastern Ross Sea (180°–150°W) has the largest decrease in sea-ice area due to outflow (3.11×10^5 km^2 yr^{-1}), and correspondingly the eastern Weddell Sea (0°E–30°E) has the largest increase in sea-ice area (2.79×10^5 km^2 yr^{-1}) from inflow.

The monthly variability of the zonal transport in Fig. 7 shows that peak transports occur in the latter half of the austral winter (August–September). The most noticeable feature is the large flow from the western Weddell Sea (60°W–30°W) to the eastern Weddell Sea (0°–30°E). The persistence of increased ice area in the Weddell Sea seen in Fig. 3 is partly due to the large inflow of sea-ice in the region through to October.

Error in the zonal transport depends linearly on the bias of ice concentration and ice velocity. Basing on the comparison between ice tracks calculated from the ice velocity data and detected from the AVHRR image, ice velocity used in this study is simply multiplied by a factor 1.4 throughout all season. After this process, there is almost no bias in the ice velocity compared with AVHRR derived ice motion. Accordingly, the error in monthly zonal transport is assumed to be small as same for *CA*.

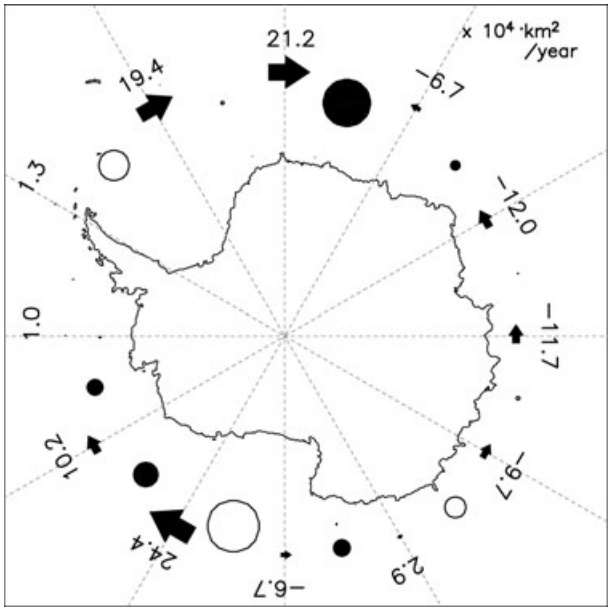

Fig. 6. Zonal transport of sea ice across 30° intervals of longitude. Digits with arrows indicate the area of the transport. Open and closed circles show the area decreased and increased through the zonal transport, respectively.

4. Processes contributing to seasonal ice area

In the previous sections, we detailed the spatial and temporal variability of the ice processes ($PI - RI$, IF and OF) governing the change of sea ice area. Using these values, this section examines the seasonal change in the net ice production at the ice edge ($PE - RE$), inferred by balancing the terms in (1).

Figure 8 shows the monthly change in ice area due to the key sea ice processes for a area defined by the 30°W and 30°E meridians. A change in ice area (*CA* shown in Fig. 2) during each month is shown by a bold line. Ice area in this sector increases from March to September as shown by positive values of *CA*. Rapid increase and decrease are observed in May and December, respectively. A thin line shows the net ice production within the sea ice ($PI - RI$), In March–July and September, $PI - RI$ takes positive values. On the other hand, ice reduction exceeds the ice production in November–January and August. A dashed line shows the net zonal inflow of sea ice ($IF - OF$) from the adjoining regions. The largest inflow is observed in September. From eq. (1), the balance of the three areas defined by $CA - (PI - RI) - (IF - OF)$ gives the net ice production at the ice edge ($PE - RE$). In Fig. 8, $PE - RE$ is positive in March–August as shown by the blue coloured area. The contribution of ice production at the ice edge is larger than the ice production within the sea ice. During March–August, the amount of increased ice area (*CA*) is 47.1×10^5 km^2 and is due to 17.2×10^5 km^2 of $PI - RI$, 26.6×10^5 km^2 of $PE - RE$, and 3.3×10^5 km^2 of $IF - OF$. The contribution of net ice production within the sea ice ($PI - RI$), net ice production at the ice edge ($PE - RE$), and net inflow from adjoining regions ($IF - OF$) to the *CA* is 37, 56 and 7%, respectively. The contribution of zonal transport ($IF - OF$) to the increase of ice area (*CA*) is clearly small compared to the thermodynamic processes of $PI - RI$ and $PE - RE$. Melting at the ice edge occurs from September to February, as shown by the red coloured area. The melting is extremely large in December with an area of 17.6×10^5 km^2 month^{-1}.

A summary of the results of this study is given in Fig. 9, which demonstrates the monthly breakdown of sea ice processes averaged over 7 yr as same for Fig. 8, for 12 regions around Antarctica divided 30° intervals in longitude. It is clear that the strength and duration of each process varies spatially around Antarctica. The key regional difference can be categorized by the strength of ice production at the ice edge ($PE - RE$) and the duration of it, as summarized in Table 2.

The seasonal change of the Weddell Sea (60°W–30°E) ice area is characterized by the long duration and large amount of $PE - RE$. It contributes to the rapid advance and large areal extent of sea ice. In the 0°–30°E region, 13.4×10^5 km^2 of $PE - RE$ occurs during 6 months, which is 53% of total increase.

Conversely, $PE - RE$ is very small around the Indian Sector (90°E–150°E), where sea ice melting occurs at the ice edge even during the advance season. In the 120°E-150°E sector, the annual amount of *PI* (13.4×10^5 km^2) is 2.8 times larger than the amount of increased ice area (positive *CA*: 4.8×10^5 km^2).

The Ross Sea (150°E–150°W) undergoes similar processes as the Weddell Sea, but produces a smaller area of ice at the edge, over a shorter duration. The contribution of positive $PE - RE$ to the increase of ice area (*CA*) is 35% (150°E–180°) and 39% (180°–150°W). Within 180°–150°W, 6.5×10^5 km^2 of ice is produced at the ice edge, mostly in March and April.

The other western region around the Amundsen-Bellingshausen Sea (120°W–60°W) has a long duration of ice production at the ice edge ($PE - RE$). $PE - RE$ become positive in March and continues to August in 90°W–60°W as shown in Fig. 9j. The sum of *PE* in this period is 5.7×10^5 km^2. 57% (120°W–90°W) and 78% (90°W–60°W) of *CA* are due to *PE*. Though the area produced at the ice edge in this region is not as large as in the Weddell Sea, the ratio of $PE - RE$ to the total increase of ice area (*CA*) is the largest of all regions around Antarctica.

Concerning the decrease of ice area, it is due to ice reduction both within the sea ice (negative $PI - RI$) and at the ice edge (negative $PE - RE$). The contribution of $PE - RE$ is larger than that of $PI - RI$ in most of regions.

The contribution of zonal transport is relatively small in all regions. However there are some cases that it plays an important role. In the eastern Weddell Sea (0°W–30°E), when ice production (both of positive $PI - RI$ and positive $PE - RE$) stops in August, there remains a large inflow of ice observed in September (1.8×10^5 km^2 month^{-1}) that leads to a continuous increase

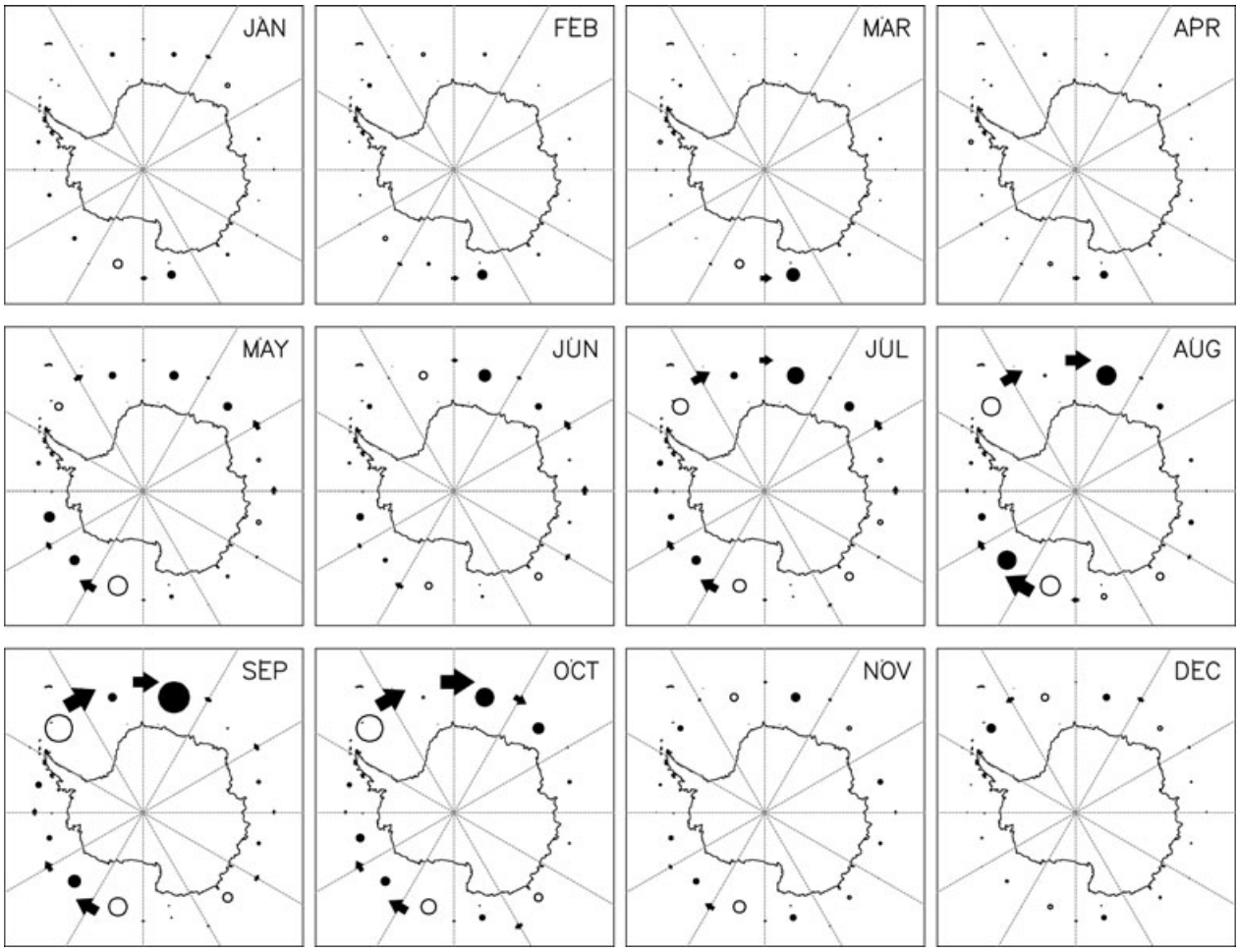

Fig. 7. Same as Fig. 6, but for each month.

in ice area (positive *CA*) until the end of September. In the eastern Ross Sea (180°–150°W), ice area begins to decrease in the middle of winter in August. The decrease in middle of summer is partly due to the outflow of ice to the east; this outflow reaches 1.2×10^5 km^2 in August.

Error assessment for $PE - RE$ is important because it is a key parameter in characterizing the regional differences in processes governing the seasonal variability of sea-ice area. The error in $PE - RE$ and the significance of the summarizing result of Fig. 9 are examined based on following method. Using the derived values of $PE - RE$, the rate of meridional advance or retreat of ice edge due to $PE - RE$ can be calculated. The derived rates are shown in Fig. 10 as a blue line, for the four specific regions of 0°E–30°E, 120°E–150°E, 180°E–150°W and 120°W–90°W. Alternatively, the same rate can be calculated directly by subtracting the meridional component of the monthly mean ice-drift speed at the ice edge from the apparent rate of advance/retreat, which is derived from the ice concentration data as the ice-edge displacement for each month. For example, if the ice edge advances from 65°S to 64°S (111 km distance) during one month, the advance rate is evaluated as 4.28 cm s^{-1}. If the mean ice-drift speed at the ice edge in this month is 3.00 cm s^{-1}, the advance rate due to ice production is 1.28 cm s^{-1}. The red lines in Fig. 10 show the advance/retreat rate due to ice production/melting at the ice edge calculated by this direct way. We can see in Fig. 10 that magnitude and temporal change of them derived from the two independent methods are very close. For example in the Weddell Sea, the longer duration and larger amount of ice production at the ice edge is derived not only by the result of Fig. 9 but also by the direct way. Similarly, the other features of the key processes in the other regions agree, that is, almost no ice production at the ice edge throughout the season between 120°E–150°E (Fig. 10b), the large ice production in March–April at the ice edge in the eastern Ross Sea (180°E–150°W, Fig. 10c), and the longer duration of ice production at the ice edge in the western Amundsen-Bellingshausen Sea (120°W–90°W, Fig. 10d). This agreement confirms that the seasonal and regional variations of $PE - RE$ discussed in this section are relevant.

It is also difficult to evaluate the error in $PI - RI$, which is sensitive to small error in the ice concentration and velocity.

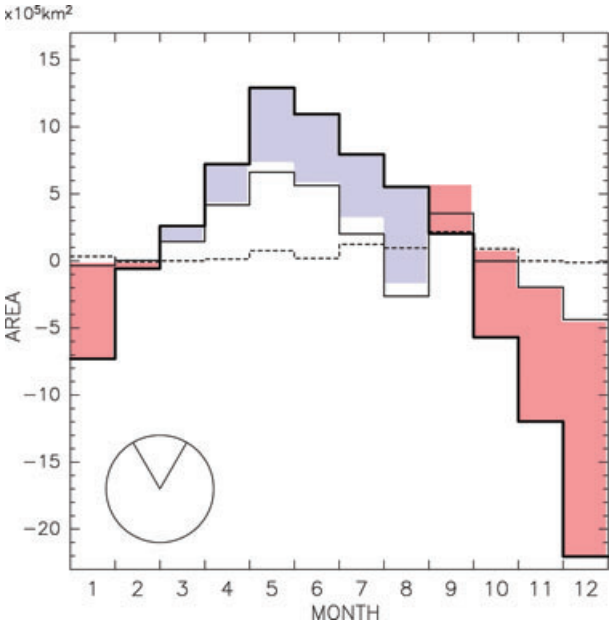

Fig. 8. Seasonal change in ice area for the region between 30°W–30°E. Bold line shows the change in sea-ice area (*CA*) during each month shown in Fig. 2. Thin line shows the net ice production within the sea ice ($PI - RI$) shown in Fig. 5. Dashed line shows the zonal inflow of sea ice ($IF - OF$) from the adjoining area (shown in Fig. 7). Light blue and red colored area is the net ice production and melting at ice edge (positive $PE - RE$ and negative), respectively. Inset shown at the lower left presents the region (30W°W–30°E) used for the plotted data.

We try to evaluate it from the error in $PE - RE$. The error in $PE - RE$ evaluated above is originated in errors of all other parameters, CA, $IF - OF$, $PI - RI$, and the ice-edge speed derived from the direct way. Major source of the derived error in $PE - RE$ is considered in the error in $PI - RI$, because errors in other parameters depend linearly on errors of sea ice concentration and/or velocity, and is not large compared with error in $PI - RI$. Here, we assume error in $PE - RE$ to be the error in $PI - RI$. Based on this assumption and employing cases that monthly $PI - RI$ is larger than 2.0×10^5 km^2, error in the monthly $PI - RI$ are evaluated as 11–29% of it. Mean of the evaluated error is 20.7% of $PI - RI$. By taking errors due to other parameters into consideration, error in $PI - RI$ seems to be smaller than this value.

5. Summary and discussion

The northward extent of the maximum ice cover varies around Antarctica, with sea ice advancing as far as 55°S in the eastern Weddell Sea (0°–30°E). Around the Amundsen-Bellingshausen Sea, the advance is limited within 65°S. With respect to the meridional distance from the coast, ice extent in the western Weddell Sea and eastern Ross Sea crosses up to 15° of latitude, whereas in the Indian Sector, ice cover is limited to a much narrower zone. These patterns of the maximum ice extent are maintained across every year. The important finding of this study is that the processes controlling the maximum ice area vary between regions.

This study examines large-scale processes governing the seasonal change in ice area over the Antarctic using AMSR-E derived daily sea-ice data. This is the first study to use the homogeneous data to reveal regional differences of the ice processes over the entire Antarctic ice area. Monthly changes in ice area (*CA*) were associated with three processes: (1) ice production/reduction within the sea ice (*PI* and *RI*), (2) ice production/reduction at the ice edge (*PE* and *RE*), and (3) the zonal transport of sea ice (*IF* and *OF*). Separation of $PE - RE$ from $PI - RI$ made the regional differences in the contribution of these processes clear. *PI*(*RI*) and *P*E(*RE*) depend on different dynamic and thermodynamic environments. Concerning an increasing ice area, the strength of *PI* is largely due to the dynamics within the sea ice pack; *PI* needs a divergence of sea ice field. Concurrently the degree of *PE* depends on the thermodynamic condition at the ice edge. Considering the contribution of these parameters, the key process for each specific region around Antarctica can be summarized as follows.

In the Weddell Sea (60°W–30°E), sea ice area increases through ice production within the sea ice(*PI*) and ice production at the ice edge (*PE*). Net ice production at the ice edge ($PE - RE$) in this area is the largest around Antarctica. Conversely, ice production in the coastal area of this region is not significant compared with other areas. Most of the *PI* is produced across the ice interior and is not concentrated in the coastal areas. In other words, ice production in lead or small opening within the sea ice plays an important role in growth of the Weddell Sea ice area. This result is basically consistent with an observation study of Eisen and Kottmeier (2000), which shows the large contribution of leads in winter ice production in the whole of the Weddell Sea. Seasonal decrease of ice area is mainly due to ice reduction at the ice edge (*RE*), though ice melting within the sea ice plays an important role in fast retreat of ice area.

The Indian Sector (90°E–150°E) is characterized by melting ice at the ice edge (*RE*) in most of months and by active ice production in the coastal areas. In this sector, $PI - RI$ exceeds *CA* even in the advance season. Sea ice is produced mainly in the coastal polynya areas, is advected offshore, and melts at the ice edge throughout the year. As such it is similar to ice process in the seasonal ice areas in the Northern Hemisphere as shown by Kimura and Wakatsuchi (2001).

The Ross Sea (150°E–150°W) ice undergoes a rapid increase in ice area in early autumn between March-April. Ice production at the ice edge (*PE*) plays an important role in the fast advance of ice area at an earlier time of the year compared with other regions. This fast advance, due to the large *PE* in early autumn, was also shown by Kimura (2007) using near infrared images of the NOAA/AVHRR. Ice production in the coastal polynya also

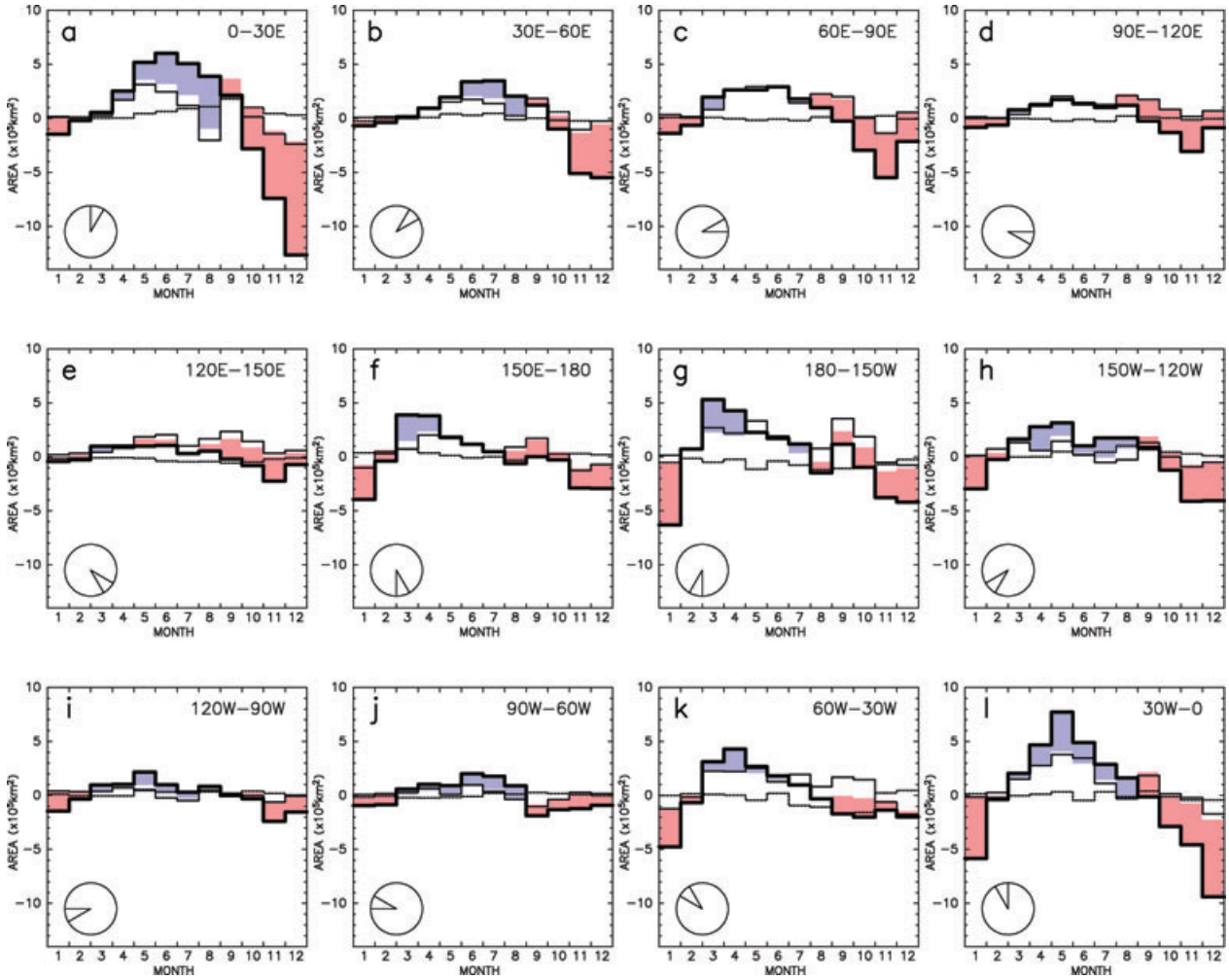

Fig. 9. Same as Fig. 8, but for each of the following areas; (a) 0°−30°E, (b) 30°E–60°E, (c) 60°E–90°E, (d) 90°E–120°E, (e) 120°E–150°E, (f) 150°E–180°, (g) 180°−150°W, (h) 150°W–120°W, (i) 120°W–90°W, (j) 90°W–60°W, (k) 60°W–30°W, (l) 30°W–0°.

contributes the ice advance; produced ice area in the coastal area reaches 75% of total positive *CA*. The Ross Sea polynya is the most active ice production region around Antarctica, consistent with the result of Orsi et al. (1999) showing that AABW with the highest salinity is formed in the Ross Sea. The ice area produced in the Ross Sea polynya is 3.6 times larger than that in the coastal polynya of Weddell Sea; this ratio is agree well with Tamura et al. (2008) showing the ratio of produced ice volume in the Ross Sea polynya to that in the coastal polynya of Weddell Sea is 4.6.

The Amundsen-Bellingshausen Sea (120°W–60°W) is different to both Ross and Weddell sectors in terms of the processes that drive ice area there. The maximum ice extent in the area is small and there is very little ice production within the sea ice (*PI*) even in the advance season. However the contribution of the ice production at the ice edge (*PE*) is largest around Antarctica. The weather conditions in this area are unfavourable for dynamic but favourable for thermodynamic expansion of the ice area. This finding is consistent with the result by Kimura (2007), which showed that sea-ice extent in this area is suppressed by the prevailing inshore wind, and that ice production at the ice edge when the wind direction moves offshore plays an important role in the advance of ice extent. Owing to this characteristic, the Amundsen-Bellingshausen Sea is sensitive to changes in climate and weather conditions. This area indeed has been identified as one of reduced ice area (Jacobs and Comiso, 1997), and where ice concentration is highly sensitive to intraseasonal and shorter time-scale changes in atmospheric conditions (Baba et al., 2006; King et al., 2010).

This study abandons a consideration of small-scale complex ice processes. Our way of estimation detects ice production/reduction based on 37.5-km-resolution daily data; it can detect ice production in the smaller scale lead or opening within the sea ice when it is due to large (more than 37.5 km) scale ice divergence. However it cannot detect ice production due to smaller scales or shorter timescales ice motion. These small-

Table 2. Duration of ice production at the ice edge ($(PE - RE) > 0$), summed $PE - RE$ during production, and the ratio of the summed $PE - RE$ to a total increase of ice area (IA: sum of CA in case of $CA > 0$) for 12 regions

	Duration (month)	PE-RE ($\times 10^5$ km^2)	(PE-RE)/IA (%)
0° − 30°E	6	13.4	53
30°E–60°E	5	5.0	38
60°E–90°E	4	1.8	14
90°E–120°E	1	0.4	6
120°E–150°E	1	0.6	13
150°E–180°	2	3.9	35
180° − 150°W	5	6.5	39
150°W–120°W	6	7.2	55
120°W–90°W	6	3.6	57
90°W–60°W	6	5.7	78
60°W–30°W	4	3.8	30
30°W–0°	6	11.4	48

scale ice phenomena, which are not detected in this study, are still essential for ice growth and decay, and directly relate to the volume of ice production (*PI*) and reduction (*RI*). Eisen and Kottmeier (2000) and Geiger and Drinkwater (2005) show diurnal and semidiurnal ice motion due to tide and internal motion are important in ice production in the Weddell Sea. In the sea, 12.4% of the ice production is owing to ice divergence with timescale of less than 30 h (Eisen and Kottmeier, 2000). Concerning the spatial resolution, small-scale ice motion with resolutions from tens centimetres affects the ice production and melting; ice motion with floe-size scale strongly affects the ice thickening and production (Toyota et al., 2004; Doble, 2009). Considering these facts, this study underestimates the ice production in interior of pack (PI) by the disregard of the small-scale ice processes. In future, the small-scale processes should be considered in examination of ice processes by analyses employing the high-resolution image. Additionally, upcoming ice thickness data from ICESat (e.g. Zwally et al., 2008) and other instruments such as ice-profiling sonar (e.g. Melling and Riedel, 1995; 1996) or electromagnetic induction (EM) devices (e.g. Haas et al., 1997; Worby et al., 1999) will enable us to detect the small-scale ice processes accompanied by the change in ice thickness. Understanding of the large-scale ice process will go ahead by taking into account the interaction between the small-scale and large-scale phenomena, and parametrization of the interactive subgrid-scale physics.

We had carried out the same analyses as this study using sea-ice data derived from SSM/I, which has a resolution twice as coarse (75 km resolution of ice velocity) as AMSR-E. There is no significant difference between overall result of this study and the SSM/I based one. Degree of *PE* derived from the SSM/I based calculation is very close to Fig. 9 of this study. One distinct difference between SSM/I derived and AMSR-E derived results is the reproducibility of coastal polynya location. The SSM/I based calculation cannot detect individual coastal polynyas around the eastern hemisphere. Zonal distribution of the coastal polynya by Stössel and Markus (2004) based on SSM/I ice concentration also cannot detect the small polynyas such as the Mertz Glacier polynya or Cape Darnley polynya detected in this study. However, this study based on AMSR-E velocity data with resolution of 37.5 km has not yet reproduce adequately the location of some coastal polynyas, which are detected in Tamura et al. (2008) based on SSM/I data with resolution of 12.5 and 25 km. For the better representation of the coastal polynya, we need finer data with resolution of 25 km or higher.

In this study, coastal polynya is mainly detected by ice divergence. The method of the detection is different from the previous studies that polynya is defined as coastal low ice-concentration area or thin ice area. Advantage of our method is that estimated polynya productivity is free from ambiguity in estimation of ice thickness or in calculation of heat exchange. Although derived productivities of polynyas in this study is nearly similar to previous studies, a method combining calculation of both static heat exchange and dynamic ice transport will make the estimation of ice production in polynya more precise.

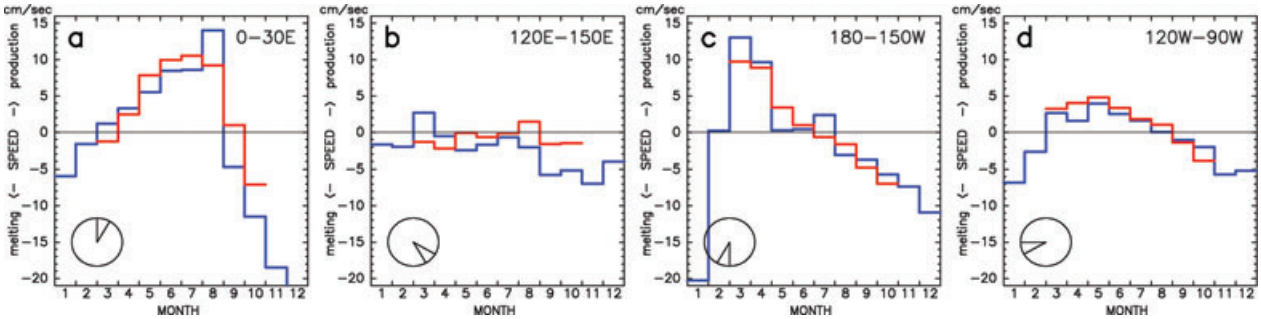

Fig. 10. Advance/retreat rate of ice edge due to ice production/melting calculated by two methods; blue line: calculated from the area of ice production/melting at the ice edge derived in Fig. 9, red line: calculated from a comparison of meridional components of ice-edge speed and ice-drift speed at the ice edge, for 0°−30°E (a), 120°E–150°E (b), 180°−150°W (c), and 120°W–90°W (d). Positive value indicates the occurrence of ice production at the ice edge.

This study highlights the ice production at the ice edge (*PE*) as a key process to characterize the regionality of ice process on the seasonal variation. Except for the Indian Sector, the process governing the seasonal increase of ice area in the Antarctic are quite different from the Northern Hemisphere (Kimura and Wakatsuchi, 2001). In the Antarctic, *PE* plays an important role in the increase of ice area and leads to a rapid advance of ice cover. In addition, we propose that *PE* is a factors suitable for checking the result of numerical models and useful to improve the models. Representation of numerical models currently is generally validated by ice area comparison (e.g. Wu et al., 2003; Chen and Yuan, 2004). However, the model performance should be validated whether it represent process of sea ice change or not. Ice production and reduction, not only *PE* but also *PI* derived in this study is useful to validate and improve the numerical model on sea ice.

In contrast to the Arctic, where summer ice area have decreased drastically (Comiso, 2002; Stroeve et al., 2005), there is no striking signal of ice decrease in the Southern Ocean (Comiso and Nishio, 2008). This study shows the apparent reduction of ice production in the Ross Sea polynya. There is a possibility that some drastic change has occurred in the Antarctic sea ice. Monitoring of ice processes such as *PI*, *RI*, *PE* and *RE* is necessary to detect the serious change in the Antarctic sea ice. We have to pay attention to the interannual change in each process governing the temporal variability of ice area.

6. Acknowledgments

We wish to thank the National Snow and Ice Data Center for the gridded AMSR-E and SSM/I data. We also thank the Kitami Institute of Technology for NOAA/AVHRR image. We acknowledge Kay I. Ohshima, Shigeru Aoki, Yasushi Fukamachi, Takenobu Toyota, Guy Williams and Takeshi Tamura for their useful comments. Much appreciation to Ray Tabesh for proofreading this document. We are very grateful to the anonymous reviewers for their comments and helpful suggestions. The figures were produced by the GFD DENNOU Library. This work was supported by the 21st-Century and Global Center of Excellence Program, and by the Grant-in-Aid 17340138 and 1871001 for scientific research, funded by the Ministry of Education, Culture, Sports, Science and Technology of Japan.

References

Baba, K., Minobe, S., Kimura, N. and Wakatsuchi, M. 2006. Intraseasonal variability of sea-ice concentration in the Antarctic with particular emphasis on wind effect. *J. Geophys. Res.* **111**, C12023, doi:10.1029/2005JC003052.

Cavalieri, D. J., Parkinson, C. L. and Vinnikov, K. Y. 2003. 30-year satellite record reveals contrasting Arctic and Antarctic decadal sea ice variability. *Geophys. Res. Lett.* **30**, 1970, doi:10.1029/2003GL018031.

Cavalieri, D. J., Markus, T., Hall, D. K., Gasiewski, A. J., Klein, M. and co-authors. 2006. Assessment of EOS Aqua AMSR-E Arctic Sea Ice Concentrations Using Landsat-7 and Airborne Microwave Imagery. *IEEE Trans. Geosci. Remote Sens.* **44**, 3057–3069.

Chen, D. and Yuan, X. 2004. A Markov model for seasonal forecast of Antarctic sea ice. *J. Clim.* **17**, 3156–3168.

Comiso, J. C. 2002. A rapidly declining Arctic perennial ice cover. *Geophys. Res. Lett.* **29**, 1956, doi:10.1029/2002GL015650.

Comiso, J. C. and Nishio, F. 2008. Trends in the sea ice cover using enhanced and compatible AMSR-E, SSM/I, and SMMR data. *J. Geophys. Res.* **113**, C02S07, doi:10.1029/2007JC004257.

Doble, M. J. 2009. Simulating pancake and frazil ice growth in the Weddell Sea: a process model from freezing to consolidation. *J. Geophys. Res.* **114**, C09003, doi:10.1029/2008JC004935.

Eisen, O. J. and Kottmeier, C. 2000. On the importance of leads in sea ice to the energy balance and ice formation in the Weddell Sea. *J. Geophys. Res.* **105**, 14 045–14 060.

Emery, W. J., Fowler, C. W., Hawkins, J. and Preller, R. H. 1991. Fram Strait satellite image-derived ice motion. *J. Geophys. Res.* **96**, 4751–4768.

Emery, W. J., Fowler, C. W. and Maslanik, J. A. 1997. Satellite derived maps of Arctic and Antarctic sea ice motion: 1988 to 1994. *Geophys. Res. Lett* **24**, 897–900.

Enomoto, H. and Ohmura, A. 1990. The influences of atmospheric half-year cycle on the sea ice extent in the Antarctic. *J. Geophys. Res.* **95**, 9497–9511.

Fichefet, T. and Maqueda, M. A. M. 1997. Sensitivity of a global sea ice model to the treatment of ice thermodynamics and dynamics. *J. Geophys. Res.* **102**, 12 609–12 646.

Geiger, C. A. and Drinkwater, M. R. 2005. Coincident buoy- and SAR-derived surface fluxes in the western Weddell Sea during Ice Station Weddell 1992. *J. Geophys. Res.* **110**, C04002, doi:10.1029/2003JC002112.

Geiger, C. A. and Perovich, D. K. 2008. Springtime ice motion in the western Antarctic Peninsula region. *Deep-Sea Res.* **55**, 338–350.

Gill, A. E. 1973. Circulation and bottom water production in the Weddell Sea. *Deep-Sea Res.* **20**, 111–140.

Gloersen, P., Campbell, W. J., Cavalieri, D. J., Comiso, J. C., Parkinson, C. L. and co-authors. 1992. Arctic and Antarctic sea ice, 1978-1987: satellite passive-microwave observations and analyses. *NASA Spec. Publ.* **511**.

Gordon, A. L., Martinson, D. G. and Taylor, H. W. 1981. The wind-driven circulation in the Weddell-Enderby basin. *Deep Sea Res.* **28**, 151–163.

Haas, C., Gerland, S., Eicken, H. and Miller, H. 1997. Comparison of sea-ice thickness measurements under summer and winter conditions in the Arctic using a small electromagnetic induction device. *Geophysics* **62**, 749–757.

Heil, P., Fowler, C. W., Maslanik, J. A., Emery, W. J. and Allison, I. 2001. A comparison of East Antarctic sea-ice motion derived using drifting buoys and remote sensing. *Ann. Glaciol.* **33**, 139–144.

Jacobs, S. S. and Comiso, J. C. 1997. Climate variability in the Amundsen and Bellingshausen Sea. *J. Clim.* **10**, 697–709.

Jacobs, S. S. and Giulivi, C. F. 2010. Large multidecadal salinity trends near the Pacific-Antarctic continental margin. *J. Clim.* **23**, 4508–4524.

Kimura, N. 2004. Sea ice motion in response to surface wind and ocean current in the Southern Ocean. *J. Meteor. Soc. Japan* **82**, 1223–1231.

Kimura, N. 2007. Mechanisms controlling the temporal variation of the sea ice edge in the Southern Ocean. *J. Oceanogr.* **63**, 685–694.

Kimura, N. and Wakatsuchi, M. 2001. Mechanisms for the variation of sea-ice extent in the Northern Hemisphere. *J. Geophys. Res.* **106**, 31 319–31 331.

Kimura, N. and Wakatsuchi, M. 2004. Increase and decrease of sea ice area in the Sea of Okhotsk: ice production in coastal polynyas and dynamic thickening in convergence zones. *J. Geophys. Res.* **109**, C09S03, doi:10.1029/2003JC001901.

King, J. C., Doble, M. J. and Holland, P. R. 2010. Analysis of a rapid sea ice retreat event in the Bellingshausen Sea. *J. Geophys. Res.* **115**, C12030, doi:10.1029/2010JC006101.

Kusahara, K., Hasumi, H. and Tamura, T. 2010. Modeling sea ice production and dense shelf water formation in coastal polynyas around East Antarctica. *J. Geophys. Res.* **115**, C10006, doi:10.1029/2010JC006133.

Markus, T. and Cavalieri, D. J. 2000. An enhancement of the NASA Team sea ice algorithm. *IEEE Trans. Geosci. Remote Sens.* **38**, 1387–1398.

Marsland, S. J., Bindoff, N. L., Williams, G. D. and Budd, W. F. 2004. Modeling water mass formation in the Mertz Glacier Polynya and Adélie Depression, East Antarctica. *J. Geophys. Res.* **109**, C11003, doi:10.1029/2004JC002441.

Massom, R. A., Stammerjohn, S. E., Lefebvre, W., Harangozo, S. A., Adams, N., and co-authors. 2008. West Antarctic Peninsula sea ice in 2005: extreme ice compaction and ice edge retreat due to strong anomaly with respect to climate. *J. Geophys. Res.* **113**, C02S20, doi:10.1029/2007JC004239.

Melling, H. and Riedel, D. A. 1995. The underside topography of sea ice over the continental shelf of the Beaufort Sea in the winter of 1990. *J. Geophys. Res.* **100**, 13 641–13 653.

Melling, H. and Riedel, D. A. 1996. Development of seasonal pack ice in the Beaufort Sea during the winter of 1991-1992: a view from below. *J. Geophys. Res.* **101**, 11 975–11 991.

Nihashi, S., Ohshima, K. I., Jeffries, M. O. and Kawamura, T. 2005. Sea-ice melting processes inferred from ice-upper ocean relationships in the Ross Sea, Antarctica.. *J. Geophys. Res.* **110**, C02002, doi:10.1029/2003JC002235.

Ninnis, R. M., Emery, W. J. and Collins, M. J. 1986. Automated extraction of pack ice motion from Advanced Very High Resolution Radiometer imagery. *J. Geophys. Res.* **91**, 10 725–10 734.

Orsi, A. H., Johnson, G. C. and Bullister, J. L. 1999. Circulation, mixing, and production of Antarctic Bottom Water. *Prog. Oceanogr.* **43**, 55–109.

Parkinson, C. L. 1992. Spatial patterns of increases and decreases in the length of the sea ice season. *J. Geophys. Res.* **97**, 14 377–14 388.

Parkinson, C. L. 1994. Spatial patterns in the length of the sea ice season in the Southern Ocean, 1979-1986. *J. Geophys. Res.* **99**, 16 327–16 339.

Rintoul, S. R. 1998. On the origin and influence of Adélie Land Bottom Water, in Ocean, Ice and Atmosphere: interactions at Antarctic Continental Margin. In: *Ocean, Ice and Atmosphere: Interactions at Antarctic Continental Margin. Antarct. Res. Ser.* Volume 75 (eds. S. S. Jacobs and R. Weiss), AGU, Washington, DC., 151–171.

Stössel, A. and Markus, T. 2004. Using satellite-derived ice concentration to represent Antarctic coastal polynyas in ocean climate models. *J. Geophys. Res.* **109**, C02014, doi:10.1029/2003JC001779.

Stroeve, J. C., Serreze, M. C., Fetterer, F., Arbetter, T., Meier, W., and co-authors. 2005. Tracking the Arctic's shrinking ice cover: Another extreme September minimum in 2004. *Geophys. Res. Lett.* **32**, L04501, doi:10.1029/2004GL021810.

Tamura, T., Ohshima, K. I. and Nihashi, S. 2008. Mapping of sea ice production for Antarctic coastal polynyas. *Geophys. Res. Lett.* **35**, L07606, doi:10.1029/2007GL032903.

Toyota, T., Kawamura, T., Ohshima, K. I., Shimoda, H. and Wakatsuchi, M. 2004. Thickness distribution, texture and stratigraphy, and a simple probabilistic model for dynamic thickening of sea ice in the southern Sea of Okhotsk. *J. Geophys. Res.* **109**, C06001, doi:10.1029/2003JC002090.

Vinnikov, K. Y., Cavalieri, D. J. and Parkinson, C. L. 2006. A model assessment of satellite observed trends in polar sea ice extents. *Geophys. Res. Lett.* **33**, L05704, doi:10.1029/2005GL025282.

Worby, A. P., Griffin, P. W., Lytle, V. I. and Massom, R. A. 1999. On the use of electromagnetic induction sounding to determine winter and spring sea ice thickness in the Antarctic. *Cold Reg. Sci. Technol.* **29**, 49–58.

Worby, A. P., Jeffries, M. O., Weeks, W. F., Morris, K. and Jana, R. 1996. The thickness distribution of sea ice and snow cover during late winter in the Bellingshausen and Amundsen Seas, Antarctica. *J. Geophys. Res.* **101**, 28 441–28 455.

Wu, X., Budd, W. F. and Allison, I. 2003. Modeling the impact of persistent Antarctic polynyas with an atmosphere-sea-ice general circulation model. *Deep-Sea Res. II* **50**, 1357–1372.

Zwally, H. J., Comiso, J. C., Parkinson, C. L., Cavalieri, D. J. and Gloersen, P. 2002. Variability of Antarctic sea ice 1979-1988. *J. Geophys. Res.* **107**, 16 327–16 339.

Zwally, H. J., Yi, D., Kwok, R. and Zhao, Y. 2008. ICESat measurements of sea ice freeboard and estimates of sea ice thickness in the Weddell Sea. *J. Geophys. Res.* **113**, C02S15, doi:10.1029/2007JC004284.